

Study of Carbon Nanotubes in Cu-Cr Metal Matrix Composites

Puneet Gill and Norman Munroe

(Submitted September 26, 2011; in revised form February 3, 2012)

A novel metal matrix composite (MMC), Cu-Cr-MWCNT (copper-chromium-multiwalled carbon nanotube), was manufactured using a powder metallurgy technique. Cu-Cr alloy is widely adopted for contacts in vacuum circuit breakers. MWCNT was incorporated in an effort to enhance electrical conductivity and decrease the usage of Cr as strategic metal. Optimized milling conditions and sintering profiles were utilized to minimize any significant damage to the MWCNTs but yet provide homogeneous distribution of all constituents. Raman spectroscopy, transmission electron microscopy (TEM), and scanning electron microscopy (SEM) were used to determine the crystal structure orientation, microstructure, and morphology, respectively, of the composite. Raman peak shift and intensity ratios assessed the stresses induced and the degree of disorder of MWCNTs in the composite. TEM indicated carbide and oxide formations in the composite. SEM images revealed the presence of MWCNTs within the metal matrix. The corrosion resistances of the composite with and without MWCNTs was determined by cyclic potentiodynamic polarization (ASTM F 2129-08) in phosphate buffer saline solution at 37 °C.

Keywords composite, corrosion, MWCNT, powder metallurgy

1. Introduction

Copper-chromium-multiwalled carbon nanotube (Cu-Cr-MWCNT) metal matrix composites (MMCs) can find application as contact material for vacuum circuit breakers (VCB) (Ref 1), electrode materials for bio-fuel cells (Ref 2), bio-sensors (Ref 3), and in implantable electrically operated devices, such as pacemakers, defibrillators, insulin pumps, drug delivery systems, etc. However, structural damage of the carbon nanotube (CNT) is often a problem encountered during their manufacture as a result of high processing temperatures and pressures associated with the production methodology. In order to retain the inherent properties of the CNTs, a methodology was adopted in this investigation to minimize damage to the outer layers. Thus, in spite of any eventual damage to the latter, the beneficial properties of the inner layers of the MWCNT are retained.

Theoretical and experimental studies on CNTs have brought to the fore their exceptional mechanical and electrical properties, as well as their ability to exhibit metallic or semiconducting behavior (Ref 4). CNTs are considered ideal for improving the mechanical properties and electrical conductivity of metal matrix composites (MMCs). However, the difficulty of distributing CNTs homogeneously in a Cu matrix has been regarded as an impeding hurdle in the fabrication of composites and many researchers have focused on solving this problem (Ref 5, 6).

The same can be said about interfacial bonding of CNTs in MMC and its influence on mechanical properties (Ref 7-9). Sun and Zhang (Ref 13) have reported weak mechanical bonding at the interface between the carbon fiber and Cu due to poor wettability (Ref 6). In addition, the generation of binding sites during fabrication has been viewed to be beneficial for interfacial bonding with the matrix (Ref 11). MWCNTs have two different areas of reactive sites: the highly reactive fullerene-like tube ends and the less reactive hexagonal cylindrical tube walls. The carbon bonds at the tip of nanotubes are under higher strain due to their larger curvature and provide an area of reactive sites and lower activation energy for oxidation reactions (Ref 11). Furthermore, local defects on the wall of the nanotubes lead to a similar reduction in the activation energy and lower oxidation temperature (Ref 12). Thus, improving the interfacial bonding between CNTs and the metal matrix has become an important feature in the development of composites with improved mechanical and electrical properties (Ref 1, 10, 13-18).

1.1 Experimental

SPEX 8000 Mixer/Mill equipment was used at a fixed milling speed of about 1200 rpm. It should be noted that the efficiency of particle size reduction is about 0.1% in a conventional ball mill, but it is considerably higher for the high-energy SPEX 8000 Mixer/Mill, where powder particles are repeatedly flattened, cold-welded, fractured, and re-welded during the milling process (Ref 19).

Pure Cu metal powder (Atlantic Equipment Engineers (AEE), 99.9% purity, 1-5 Micron) and Cr metal powder (AEE, 99.8% purity, 1-5 μm) were milled in a hardened stainless steel vial (diameter 21/4 in. \times 3 in.) under an inert atmosphere (Argon). In order to limit agglomeration and sticking on the grinding media, the milled powder was scraped at regular intervals. An optimized milling and cooling regime was developed in this investigation to minimize temperature

Puneet Gill and Norman Munroe, Department of Mechanical & Materials Engineering, Florida International University, 10555 West Flagler Street, Miami, FL 33174. Contact e-mail: pgill001@fiu.edu.

rise and damage to the CNTs, and yet achieve its homogeneous distribution. Cu-Cr powders were ball milled employing 1/2 in. stainless steel balls at a 10:1 ball to powder ratio (BPR). MWCNTs (NanoAmor, 99% purity, OD 40-60 nm) were ball milled using 1/4 in. stainless steel balls at a 3:1 BPR in an effort to minimize the degree of damage to the MWCNTs. A homogeneous distribution of CNTs was achieved by conducting preliminary tests, where the milling time, BPR, and ball size were varied, and the milled powders were analyzed by SEM/mapping and Raman Spectroscopy (Ref 1, 18).

The work-hardened powders were cold compacted in an evacuable stainless steel-hardened pellet die (844 MPa) using a Carver manual press with a hold time of 90 min. The green compacts were then sintered at three different temperatures (750, 900, and 1050 °C) under argon with a ramp time of 30 min, a holding time of 150 min, followed by furnace cooling.

Raman spectroscopy (Spectra Physics, model 177G02) of spectral resolution 4 cm^{-1} with an argon ion laser of wavelength 514.5 nm was used to evaluate any lattice damage of MWCNTs during fabrication. MWCNTs usually exhibit tangential stretching with a characteristic D band ($\sim 1350\text{ cm}^{-1}$) and G band ($\sim 1500\text{--}1600\text{ cm}^{-1}$) Raman shift (Ref 20-23). The D band is a double-resonance Raman mode, which can be understood as a measurement of structural disorder developed from defects in graphite-like materials (Ref 20, 21). The G band originates from the tangential in-plane stretching vibrations of the carbon-carbon bonds within the graphene sheets (Ref 20, 21). The ratio of intensities of the D and G bands, $R = I_D/I_G$, can be used to evaluate the disorder density in the crystal structure of MWCNTs. A peak shift confirms the presence of either compressive or tensile stresses within the crystal structure of the composite, which can occur during ball milling, compaction, sintering, and compositional changes. The D and G peaks were evaluated using the full-width half-maximum (FWHM) parameter, which is a measure of the average width of the spectra.

The microstructure, space group symmetries, and morphology/elemental mapping of the composite were determined

using TEM (Philips CM200) and SEM (JEOL JSM 6330F), respectively.

Corrosion tests were conducted in phosphate buffer saline (PBS) at 37 °C using a GAMRY[®] potentiostat (G-750) equipped with an Instrument Framework Software and employing a scan rate of 1 mV/s over a potential range of -0.5 to $2.5\text{ V}_{\text{SCE}}$. The tests were conducted in compliance with ASTM F 2129-08 (Ref 29).

2. Results and Discussion

Previous attempts to prepare the composite utilizing a variety of milling parameters indicated significant MWCNT damage. By using Raman spectroscopy, it was possible to optimize the milling parameters so as not to compromise the properties of MWCNT. Similarly, optimum sintering conditions were also determined from Raman spectroscopy data by comparing the spectra of the as received MWCNT before and after sintering, as well as those of the compacts before and after sintering under argon. The sintering of pure MWCNT was conducted to determine the effect of temperature on its Raman spectra parameters. Table 1 compares the ratio of I_D/I_G (R) of the as-received MWCNTs ($R = 0.9$) with that of sintered MWCNTs ($R = 0.7$). It can also be observed that there was no variation in R with increasing temperature from 750 to 1050 °C for sintered MWCNT. However, entrapped air within the MWCNTs may have caused its partial oxidation resulting in the formation of carboxyl and carbonyl groups on the surface of the nanotubes (Ref 24), which would affect the breathing motion of the sp^2 rings and tangential vibration of the carbon bonds, resulting in $R = 0.7$. Graphitized MWCNTs have been shown to exhibit a value of ~ 1.1 (Ref 12).

Table 2 compares R (0.9-1.1) and Raman spectral shift of various compositions of green compacts. A relatively constant R was indicative of no significant change in the structure of MWCNT during ball milling and compaction. The Raman shifts obtained for the compacts were in the ranges of

Table 1 Raman spectra parameters of as-received and sintered MWCNT

Sintering temperature, °C	D band, cm^{-1}		G band, cm^{-1}		Ratio (R) = I_D/I_G
	Position	FWHM	Position	FWHM	
750	1346	50.8	1571	41.0	0.7
900	1348	56.3	1575	39.8	0.7
1050	1340	37.6	1567	41.4	0.7
Unsintered MWCNT	1355	61.4	1581	48.1	0.9

Table 2 Raman spectra parameters of green composites

Composition, vol.%	D band, cm^{-1}		G band, cm^{-1}		$R = I_D/I_G$
	Position	FWHM	Position	FWHM	
Cu-15Cr-8MWCNT	1361	44.3	1587	32.8	1.1
Cu-14Cr-10MWCNT	1356	36.2	1587	37.3	1.0
Cu-13Cr-12MWCNT	1345	51.4	1581	47.5	1.0
Cu-12Cr-14MWCNT	1357	52.1	1587	39.7	0.9
Cu-11Cr-16MWCNT	1347	38.4	1573	53.7	0.9

1345-1361 cm^{-1} and 1573-1587 cm^{-1} for D and G bands, respectively, which indicated that minimal stress was introduced during ball milling and compaction and that structural uniformity was maintained.

Table 3 shows Raman spectra of composites sintered under argon at three temperatures 750, 900, and 1050 °C. The MWCNT content within the fired composite and the sintering temperature had no significant effects on R and Raman shift. Furthermore, the retention of crystal structure of MWCNTs in the composite was confirmed by the D ($\sim 1340 \text{ cm}^{-1}$) and G peaks ($1500\text{-}1600 \text{ cm}^{-1}$), which were similar to those obtained for as received MWCNTs. These results, therefore, indicated minimal damage to MWCNTs during milling, compaction, and sintering of the composite.

Typical Raman spectra of MWCNTs for different sintering temperatures and compositions can be expressed in terms of FWHM values (see Tables 1-3). The Raman spectrum of as-received MWCNTs had a FWHM of 61.4 (D band) and 48.1 (G band), which were similar to those reported by Sebastian 54.9 and 45.6, respectively (Ref 12). These values decreased after sintering to (56.1-41.2 D band) and (53.6-31.5 G band), which were again similar to those reported by Sebastian 41.0 and 36.5, respectively. Therefore, a lowering of the FWHM for D and G bands confirmed the graphitization of MWCNTs upon sintering under argon.

Figure 1 shows the peak intensity versus the Raman shift curves for various compositions of MWCNT MMC composites at different sintering temperatures. The vertical line serves to indicate no significant Raman shift, which was an indication of minimal induced stress and disorder in the MWCNT MMC. The G band varied between 1570 and 1590 cm^{-1} , which may have been due to non-uniformity in the size of the nanotubes, varying defect density, tube bundling, and rough surface of the compacts. The values of R, which varied between 0.7 and 1.3 may have also resulted from the aforementioned features.

Figure 2(a) illustrates a bright field TEM photomicrograph of the composite. Figure 2(b) shows the indexed diffraction spots corresponding to the polycrystalline phases developed in the Cu-Cr-MWCNT composite. From a thermodynamic perspective, some chromium carbide formation can be expected ($\Delta G = -15 \text{ kcal/mol}$), which was confirmed by the TEM diffraction data shown in Fig. 2(b). It was postulated that the

highly reactive edges and broken surfaces of the MWCNT served as reactive sites for the formation of carbides via bonding mechanisms, such as chain-link structures, Y-junctions, rope anchors, and bridges (Ref 1). The MWCNT bonds with Cr as a carbide at highly reactive sites, whereas some Cr become engulfed as solute in the Cu matrix. The selected area diffraction (SAD) ring pattern (Fig. 2b) confirms the formation of chromium carbide. This interfacial bonding mechanism producing chromium carbide is believed to be responsible for the enhanced mechanical properties of the composite, such as wear resistance and corrosion resistance.

The SAD pattern shown in Fig. 2(b) also confirmed the formation of two common forms of copper oxide: cupric oxide or monoclinic tenorite (CuO); and cubic cuprous oxide or cuprite (Cu_2O), which are both p-type semiconductors with band gaps of 1.9-2.1 and 2.1-2.6 eV, respectively (Ref 25-27). The oxide formation may have been caused by infiltration of air during compaction of the green composite.

The morphology of the composite was examined by SEM. The photomicrograph in Fig. 3 confirms the retention of MWCNTs in the composite even after harsh fabrication conditions, such as milling, compaction, and sintering.

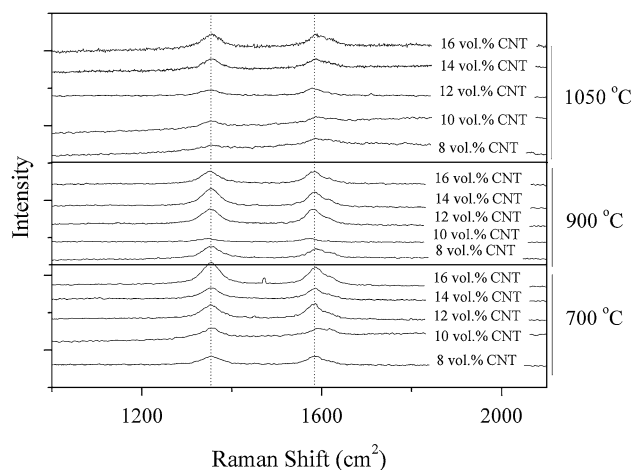


Fig. 1 Raman spectra of composites at different sintering temperatures

Table 3 Raman spectra parameters of sintered composite

Sintering temperature, °C	Composition, vol.%	D band, cm^{-1}		G band, cm^{-1}		$R = I_D/I_G$
		Position	FWHM	Position	FWHM	
750	Cu-15Cr-8MWCNT	1357	61.0	1587	38.5	0.9
	Cu-14Cr-10MWCNT	1361	42.5	1588	31.5	0.9
	Cu-13Cr-12MWCNT	1356	37.5	1581	47.9	1.0
	Cu-12Cr-14MWCNT	1361	46.2	1588	32.7	1.1
	Cu-11Cr-16MWCNT	1356	41.2	1587	39.6	1.1
900	Cu-15Cr-8MWCNT	1337	56.1	1577	43.3	0.9
	Cu-14Cr-10MWCNT	1350	52.5	1589	71.6	1.1
	Cu-13Cr-12MWCNT	1340	47.5	1571	40.9	1.0
	Cu-12Cr-14MWCNT	1356	41.3	1587	34.3	1.1
	Cu-11Cr-16MWCNT	1353	41.3	1587	53.6	1.3
1050	Cu-15Cr-8MWCNT	1342	49.2	1587	35.1	1.2
	Cu-14Cr-10MWCNT	1361	48.6	1594	61.5	0.7
	Cu-13Cr-12MWCNT	1355	43.8	1587	47.9	0.9
	Cu-12Cr-14MWCNT	1357	53.7	1590	44.3	1.0
	Cu-11Cr-16MWCNT	1361	41.2	1590	33.7	1.0

Figure 4 illustrates the surface distribution of Cu, Cr, and MWCNTs in the composite. The elemental mapping analyses revealed good distribution of MWCNTs in the metal matrices.

Figure 5 shows the cyclic potentiodynamic polarization curves for Cu-18Cr vol.% and Cu-14Cr-10MWCNT vol.% sintered at 900 °C. The Cu-Cr exhibited a tri-stage passivation behavior followed by a hysteresis loop during the reverse

potential scan, i.e., the curve looped in an anticlockwise direction. The resistance to pitting corrosion was evaluated by measuring the difference between breakdown and rest potentials ($E_b - E_r$) during the first stage of passivation. The Cu-Cr-MWCNT also exhibited a current reversal in an anti-clockwise direction, but without a hysteresis loop. A typical cyclic potentiodynamic curve is shown in the inset of Fig. 5 (Ref 28),

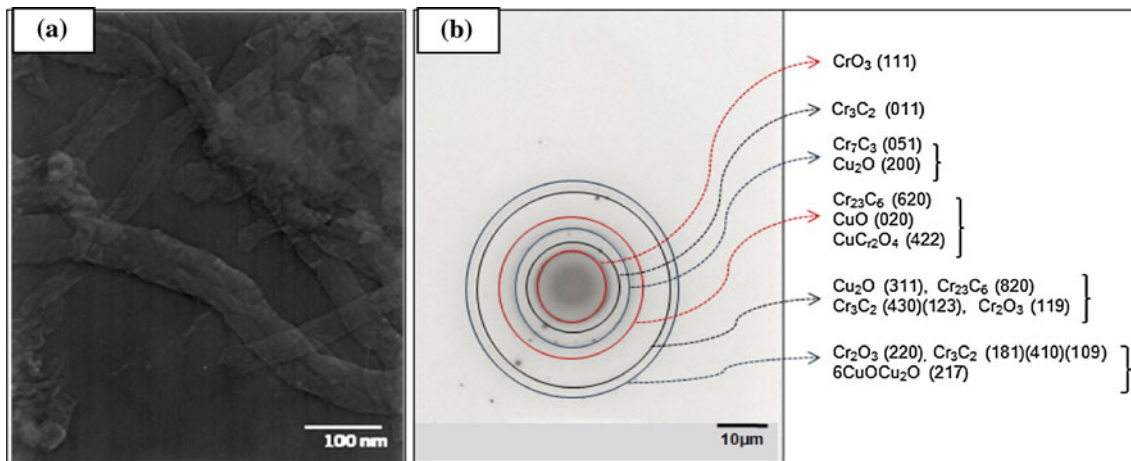


Fig. 2 (a) TEM photomicrograph depicting dispersion of Cu-Cr-MWCNT and (b) SAD ring pattern indexed for different phases in the composite

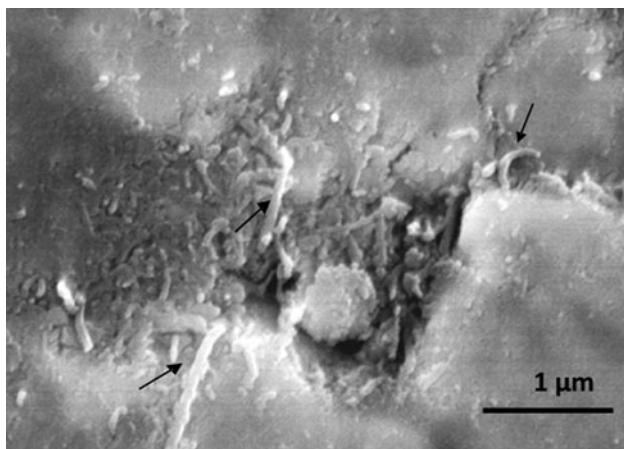


Fig. 3 SEM photomicrograph of Cu-14Cr-10MWCNT vol.% composite sintered at 900 °C

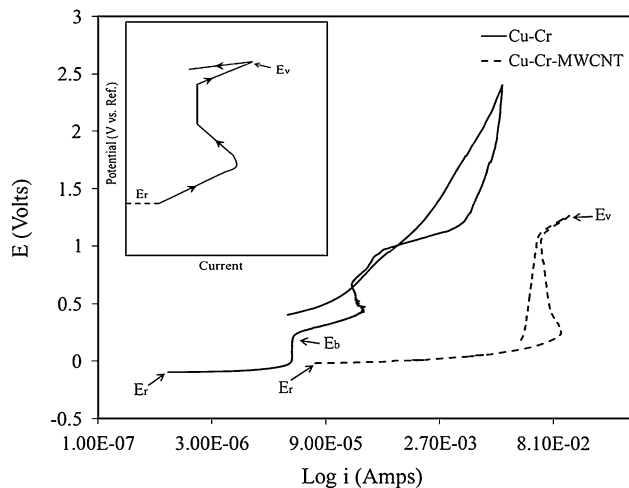


Fig. 5 Cyclic potentiodynamic curves for Cu-Cr and Cu-Cr-MWCNT composite (inset shows a typical cyclic potentiodynamic curve; Ref 29)

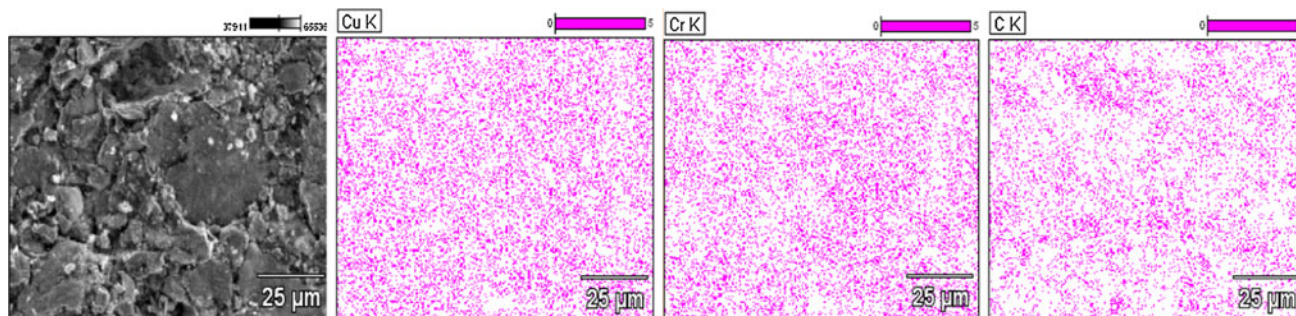


Fig. 4 Mapping of Cu-14Cr-10MWCNT vol.% sintered at 900 °C

Table 4 Average corrosion parameters for Cu-Cr and Cu-Cr-MWCNT composites

Composition, vol.%	Cyclic potentiodynamic polarization parameters, V			
	E_b	E_r	E_v	$E_b - E_r$
Cu-18Cr	0.325	-0.081	NA	0.406
Cu-14Cr-10MWCNT	NA	-0.058	1.377	NA

for materials where oxygen evolution occurs at E_v . A large hysteresis loop is indicative of the degree of difficulty for a material to passivate after the passive film is disrupted. The Cu-Cr-MWCNT composite exhibited no hysteresis loop, in which case, the corrosion resistance was evaluated by the vertex potential E_v . Table 4 shows the corrosion parameters for the Cu-Cr alloy ($E_b - E_r = 0.406$ V) and Cu-Cr-MWCNT ($E_v = 1.377$ V). It is apparent that the addition of MWCNTs enhanced the passivation of the alloy via the formation of carbides (see Fig. 2b) at the highly reactive edges and broken surfaces of MWCNTs as previously discussed.

3. Conclusions

MWCNTs were successfully incorporated into the Cu-Cr alloy with minimal structural destruction using a cost-effective powder metallurgy technique. The non-uniformity in size of the nanotubes, varying defect density, tube bundling, and rough sample surface affected the D and G peak shifts and the I_D/I_G ratio. Elemental mapping indicated that the distribution of MWCNT in the MMC was relatively homogeneous. The results of Raman spectroscopy, TEM, and SEM analyses indicated minimal damage to MWCNTs under optimized milling, compaction, and sintering conditions. A minor amount of chromium carbide was also produced, the formation of which may have served to improve the strength of the composite by providing a variety of interfacial bonding mechanisms with MWCNT. The incorporation of MWCNTs into the Cu-Cr metal matrix resulted in an increased resistance to pitting corrosion.

References

1. N. Munroe, P.K.S. Gill, S. Amruthaluri, and W. Haider, Highly Conductive Nanostructured Cu-Cr-MWCNT Composite, *Materials Science and Technology (MS&T) Conference & Exhibition*, 2008, p 2309–2318
2. N. Munroe, P.K.S. Gill, S. Amruthaluri, C. Pullettikurti, and W. Haider, MWCNT Based Metal Matrix Composite for Micro-Bio-Fuel Cells, *Knowledge Foundation's International Symposium—Portable Energy*, 2009
3. S. Akar, V. Tek, A. Bange, L. Lagos, P. Gill, N. Munroe, and T.G. Thundat, Development of a Biosensor for Detection of Phosphate Species in Uranium Contaminated Ground Water and Wastewater Sediments, *Waste Management Conference* (Phoenix, AZ), 2010
4. B. Miao, Y. Zhang, and G. Liu, *Current Status and Developing Trends, of Cu-Cr Manufacturing Technique Contact Materials for VCB*, 2004, IEEE:0-7803-8461-X/04-2004
5. A. Peigney, E. Flahaut, C. Laurent, F. Chastel, and A. Rousset, Aligned Carbon Nanotubes in Ceramic-Matrix Nanocomposites Prepared by High-temperature Extrusion, *Chem. Phys. Lett.*, 2005, **352**, p 20–25
6. E. Flahaut, A. Peigney, C.H. Laurent, C.H. Marlière, F. Chastel, and A. Rousset, Carbon Nanotubes-Metaloxide Nanocomposites: Microstructure,

Electrical Conductivity and Mechanical Properties, *Acta Mater.*, 2000, **48**, p 3803–3812

7. D.A. Mortimer and M. Nicholas, The Wetting of Carbon by Copper and Copper Alloys, *J. Mater. Sci.*, 1970, **5**, p 149–155
8. S.I. Cha, K.T. Kim, S.N. Arshad, C.B. Mo, and S.H. Hong, Extraordinary Strengthening Effect of Carbon Nanotubes in Metal-Matrix Nanocomposites Processed by Molecular-Level Mixing, *Adv. Mater.*, 2005, **17**, p 1377–1381
9. J.M. Casstevens, H.G. Rylander, and Z. Eliezer, Influence of High Velocities on the Friction of Copper-Graphite Brushes, *Wear*, 1978, **48**, p 121–130
10. X. Wang, N.P. Padture, and H. Tanaka, Contact-Damage-Resistant Ceramic/Single-Wall Carbon Nanotubes and Ceramic/Graphite Composites, *Nat. Mater.*, 2004, **3**, p 539–544
11. P.K.S. Gill, "Synthesis and Investigation of Highly Conductive Cu-Cr-MWCNT Composites," Thesis, Florida International University, Miami, FL, 2008
12. S. Kanchibhotla, "Study on Amorphization of Ni-Ti-Ta System & Production of NiTi-Ta Alloys Through Conventional Powder Metallurgy," Thesis, Florida International University, Miami, FL, 2004
13. S.J. Sun and M.D. Zhang, Interface Characteristics and Mechanical Properties of Carbon Fibre Reinforced Copper Composites, *J. Mater. Sci.*, 1991, **26**, p 5762–5766
14. G.D. Zhan, J.D. Kuntz, J. Wan, and A.K. Mukherjee, Single-Wall Carbon Nanotubes as Attractive Toughening Agents in Alumina-based Nanocomposites, *Nat. Mater.*, 2003, **2**, p 38–42
15. C.S. Goh, J. Wei, L.C. Lee, and M. Gupta, Simultaneous Enhancement in Strength and Ductility by Reinforcing Magnesium with Carbon Nanotubes, *Nanotechnology*, 2006, **17**, p 7–12
16. K.T. Lau, C. Gu, and D. Hui, A Critical Review on Nanotube and Nanotube/Nanoclay Related Polymer Composite Materials, *Compos. B Eng.*, 2006, **37**, p 425–436
17. W.X. Chen, J.P. Tu, L.Y. Wang, H.Y. Gan, Z.D. Xu, and X.B. Zhang, Tribological Application of Carbon Nanotubes in a Metal-Based Composite Coating and Composites, *Carbon*, 2003, **41**, p 215–222
18. R.A. Graff, J.P. Swanson, P.W. Barone, S. Baik, D.A. Heller, and M.S. Strano, Achieving Individual-Nanotube Dispersion at High Loading in Single-Walled Carbon Nanotube Composites, *Adv. Mater.*, 2005, **17**, p 980–984
19. E.G. Rakov, *Nanomaterials Handbook*, Y. Gogotsi, Ed., CRC Press, Boca Raton, 2006,
20. S. Osswald, M. Havel, and Y. Gogotsi, Monitoring Oxidation of Multiwalled Carbon Nanotubes by Raman Spectroscopy, *J. Raman Spectrosc.*, 2007, **38**(6), p 728–736
21. A. Jorio, R. Saito, G. Dresselhaus, and M.S. Dresselhaus, Determination of Nanotubes Properties by Raman Spectroscopy, *Philos. Trans. R. Soc. London Ser. A*, 2004, **362**, p 2311–2336
22. M.S. Dresselhaus, G. Dresselhaus, R. Saito, and A. Jorio, Raman Spectroscopy of Carbon Nanotubes, *Phys. Rep.*, 2005, **409**, p 47–99
23. A.M. Rao, E. Richter, S. Bandow, B. Chase, P.C. Eklund, K.A. Williams, S. Fang, K.R. Subbaswamy, M. Menon, A. Thess, R.E. Smalley, G. Dresselhaus, and M.S. Dresselhaus, Diameter Selective Raman Scattering from Vibrational Modes in Carbon Nanotubes, *Science*, 1997, **275**, p 187–191
24. C. Thomsen, S. Reich, and J. Maultzsch, Resonant Raman Spectroscopy of Nanotubes, *Philos. Trans. R. Soc. London Ser. A*, 2004, **362**, p 2337–2359
25. A.C. Ferrari, A Model to Interpret The Raman Spectra of Disordered, Amorphous and Nanostructured Carbons, *Material Research Society Symp. Proc.*, Vol. 675, 2001
26. S.C. Ray, Preparation of Copper Oxide Thin Film by the Sol-Gel-Like Dip Technique and Study of Their Structural and Optical Properties, *Sol. Energy Mater. Sol. Cells*, 2001, **68**, p 307–312
27. J.F. Pierson, A. Thobor-Keck, and A. Billard, Cuprite, Paramelaconite and Tenorite Films Deposited by Reactive Magnetron Sputtering, *Appl. Surf. Sci.*, 2003, **210**, p 359–367
28. B. Balamurugan and B.R. Mehta, Optical and Structural Properties of Nanocrystalline Copper Oxide Thin Films Prepared by Activated Reactive Evaporation, *Thin Solid Films*, 2001, **396**, p 90–96
29. ASTM F 2129-08, Standard Test Method for Conducting Cyclic Potentiodynamic Polarization Measurements to Determine the Corrosion Susceptibility of Small Implant Devices, *Annual Book of ASTM Standards*